Chem Biol Drug Des 2015; **86:** 1072–1086

Research Article

Re(I) and Tc(I) Complexes for Targeting Nitric Oxide Synthase: Influence of the Chelator in the Affinity for the Enzyme

Bruno L. Oliveira[1,*,†], Maurício Morais[1], Filipa Mendes[1], Irina S. Moreira[2], Carlos Cordeiro[3], Pedro A. Fernandes[2], Maria J. Ramos[2], Roger Alberto[4], Isabel Santos[1] and João D. G. Correia[1,*]

[1]*Centro de Ciências e Tecnologias Nucleares, Instituto Superior Técnico, Universidade de Lisboa, Estrada Nacional 10 (ao km 139,7), Bobadela LRS 2695-066, Portugal*
[2]*Departamento de Química e Bioquímica, Faculdade de Ciências da Universidade do Porto, REQUIMTE, Rua do Campo Alegre, Porto 4169-007, Portugal*
[3]*Departamento de Química e Bioquímica, Faculdade de Ciências da Universidade de Lisboa, Campo Grande, Lisboa 1749-016, Portugal*
[4]*Department of Chemistry, University of Zurich, Winterthurerstrasse 190, Zurich CH-8057, Switzerland*
**Corresponding author: João D. G. Correia, jgalamba@itn.pt; Bruno L. Oliveira, oliveira@nmr.mgh.harvard.edu*
†Current address: A. A. Martinos, Center for Biomedical Imaging, Massachusetts General Hospital and Harvard Medical School, 149 13th Street, Suite 2301, Charlestown, MA 02129, USA

Aiming to design ^{99m}Tc complexes for probing nitric oxide synthase (NOS) by SPECT, we synthesized conjugates (L4–L6) comprising a NOS-recognizing moiety connected to a diamino-propionic acid (dap) chelating unit. The conjugates led to complexes of the type fac-[M(CO)$_3$(κ^3-L)] (M = Re/^{99m}Tc; Re4/Tc4: L = L4; Re5/Tc5: L = L5; Re6/Tc6: L = L6). Enzymatic studies showed that L4 and L5, but not L6, gave complexes (Re4 and Re5) that are less potent than the conjugates. To rationalize these results, we performed docking and molecular dynamics simulations. The high affinity of L4 and L5 is due to the strong interactions between the dap chelator and polar residues of the binding cavity. These interactions are hampered by metallation resulting in complexes with lower affinity. The higher potency of Re5 compared to Re4 was assigned to the increased bulkiness of Re5 and the presence of additional anchoring groups that better fit the active site and provide more extensive contacts. In turn, Re6 is too bulky and its organometallic tail is oriented toward the peripheral pocket of iNOS, leading to loss of contacts and a lower affinity. These results were compared with our previous results obtained with analogue complexes stabilized by a pyrazolyl-diamine chelating unit.

Key words: docking, molecular dynamics, nitric oxide synthase, rhenium and technetium

Received 30 December 2014, revised 26 March 2015 and accepted for publication 12 April 2015

Nitric oxide (NO) is a mammalian signaling molecule biosynthesized by NO synthases (NOS), which comprise three distinct isoforms: neuronal NOS (nNOS or NOSI), inducible (iNOS or NOSII), and endothelial NOS (eNOS or NOSIII). Besides being involved in a variety of physiological processes that include vasorelaxation, neurotransmission, and cytotoxicity, the localized overproduction of NO resulting from NOS upregulation has also been associated to cancer, neurological disorders, or vascular malfunctions, among others (1–4). In the past years, there has been growing clinical evidence that associates iNOS with tumor progression and angiogenesis (3,5,6). These results validate iNOS as a promising molecular target for therapy and/or imaging of tumors. The *in vivo* molecular imaging of iNOS by non-invasive modalities such as the nuclear imaging techniques positron emission tomography (PET) and single photon emission computed tomography (SPECT) holds great potential for the detection and staging of NO/iNOS-related cancers (7–13). So far, the main modalities explored for NOS imaging include PET and optical imaging. In view of our interest in the design of ^{99m}Tc(I)-based radioactive probes for molecular imaging by SPECT, we already introduced a family of complexes of the type *fac*-[M(CO)$_3$(κ^3-L)]$^+$ (M = ^{99m}Tc or Re; **Tc1**/**Re1**: L = **L1**; **Tc2**/**Re2**: L = **L2**; **Tc3**/**Re3**: L = **L3**) with pendant NOS-recognizing moieties (Figure 1). The surrogate complexes **Re1**–**Re3**, based on natural rhenium, present moderate (**Re1**, $K_i = 257\ \mu\text{M}$; **Re2**, $K_i = 84\ \mu\text{M}$) to high affinity (**Re3**, $K_i = 6\ \mu\text{M}$) for purified iNOS, being in the case of **Re3** similar to that of the free non-conjugated inhibitor N^{ω}-NO$_2$-L-arginine ($K_i = 3$–$8\ \mu\text{M}$). Moreover, all complexes permeate through RAW 264.7 macrophage cell membranes, interacting specifically with the target enzyme, as confirmed by the suppression of NO biosynthesis in lipopolysaccharide (LPS)-treated macrophages (**Re1**: ca. 20% inhibition; **Re2**: ca. 30% inhibition; **Re3**: ca. 50% inhibition) and internalization studies with **Tc1**–**Tc3** with the same cell model (14–16).

doi: 10.1111/cbdd.12575

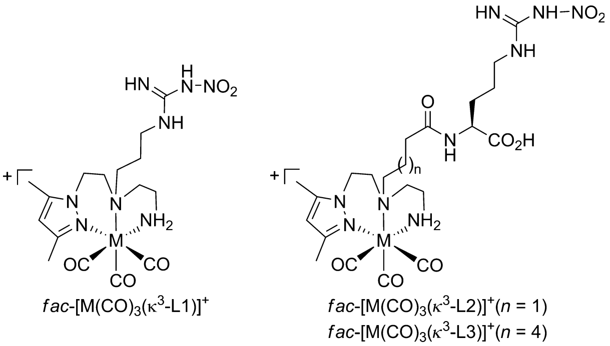

Figure 1: Complexes of the type *fac*-[M(CO)$_3$(κ^3-L)] (M = ^{99m}Tc/Re; **Tc1/Re1**: L = **L1**; **Tc2/Re2**: L = **L2**; **Tc3/Re3**: L = **L3**).

Biodistribution studies in LPS-pretreated C57BL6 mice have shown that **Tc2** accumulates in lung, which is known to be the organ with the highest iNOS expression after LPS treatment (15). Altogether, these promising results prompted us to explore a new family of ^{99m}Tc(I) complexes stabilized by bifunctional 2,3-diamino-propionic acid (dap)-based chelators. The small size of the dap-derived chelators gives 'M(CO)$_3$' complexes (M = ^{99m}Tc, Re) with physicochemical characteristics, namely hydrophilicity, optimally compatible with the requirements for *in vivo* imaging applications (17,18). Additionally, it has been also clearly demonstrated that small molecules can be labeled with ^{99m}Tc (I) using the dap chelator under the retention of transporter and receptor affinity (19–22). In this way, we anticipated that dap-derived chelators would allow the labeling of low molecular weight pharmacophores such as N^{ω}-NO$_2$-L-arginine derivatives, giving organometallic complexes with adequate pharmacokinetics and different structural properties, which could result in an improved ability to recognize the iNOS enzyme. Thus, herein we describe the synthesis and characterization of novel 'M(CO)$_3$' complexes stabilized by dap derivatives containing pendant propyl-NO$_2$-guanidino or N^{ω}-NO$_2$-L-arginine moieties for iNOS recognition, connected to the dap chelator via different spacers. We will also report on the enzymatic activity of iNOS in the presence of the compounds and assess their ability to influence NO biosynthesis in LPS-activated macrophages. The results obtained are combined with molecular modeling of the complexes to shed light on the structural determinants responsible for the different affinities.

Methods and Materials

Chemicals and solvents of reagent grade were purchased from Aldrich and used without further purification. *tert*-Butyl 2-acetamido-2-cyanoacetate (**1**, Supporting Information) and [Re(H$_2$O)$_3$(CO)$_3$]Br were prepared according to published methods (23–25). All reactions were carried out under N$_2$. NMR spectra were recorded on Varian Mercury 200 MHz, Varian Gemini 300 MHz, or Bruker 500 MHz instrument. ^{1}H and ^{13}C chemical shifts were referenced with the residual solvent resonances relatively to tetramethylsilane. The spectra were fully assigned with the help of 2D experiments (^{1}H–^{1}H correlation spectroscopy, gCOSY, and ^{1}H-^{13}C heteronuclear single quantum coherence, HSQC). Infrared spectra (IR) were recorded as KBr pellets on a Bruker Tensor 27 spectrometer. All compounds were characterized by electrospray ionization mass spectrometry (ESI-MS) using a Bruker model Esquire 3000 plus. HPLC analyses were performed on a Perkin Elmer LC pump 200 coupled to a Shimadzu SPD 10AV UV-Vis and to a Berthold-LB 509 radiometric detector, using an analytical Macherey-Nagel C18 reversed-phase column (Nucleosil 100-10, 250 × 4 mm) with a flow rate of 1 mL/min. Purification of the rhenium compounds was achieved on a semi-preparative Macherey-Nagel C18 reversed-phase column (Nucleosil 100-7, 250 × 8 mm) with a flow rate of 2.0 mL/min. UV detection: 254 or 220 nm. HPLC solvent eluent A was aqueous 0.1% CF$_3$CO$_2$H (TFA) and eluent B was MeOH. HPLC gradient: t = 0–3 min, 0% B; 3–3.1 min, 0→25% B; 3.1–9 min, 25% B; 9–9.1 min, 25→34% B; 9.1–20 min, 34→100% B; 20–25 min, 100% B; 25–25.1 min, 100→0% B; and 25.1–30 min, 0% B. Na[^{99m}TcO$_4$] was eluted from a ^{99}Mo/^{99m}Tc generator using 0.9% saline. The radioactive precursor *fac*-[^{99m}Tc(H$_2$O)$_3$(CO)$_3$]$^+$ was prepared using a IsoLink® kit (Mallinckrodt, Covidien). NOS assays were recorded on an Agilent Technologies 8453 UV-Vis diode array spectrophotometer with a thermostated multicuvette holder with stirring. The iNOS (mouse recombinant enzyme), bovine hemoglobin, β-nicotinamide adenine dinucleotide 2-phosphate reduced tetrasodium salt hydrate (NADPH), tetrahydrobiopterin (BH$_4$), 4-(2-hydroxyethyl) piperazine-1-ethanesulfonic acid (HEPES), and DL-dithiothreitol (DTT) were purchased from Sigma-Aldrich.

2-Amino-2-(aminomethyl)-5-(3-nitroguanidino) pentanoic acid (L4)

To a stirred solution of **1** (55 mg, 0.166 mmol) in anhydrous EtOH were added Et$_3$N (100 mg, 0.996 mmol) and 2-methyl-1-nitro-2-thiopseudourea (68 mg, 0.498 mmol), which was prepared as previously described (14). The reaction temperature was then raised to 40 °C, and stirring continued overnight under nitrogen atmosphere. The solvent was evaporated under reduced pressure, and the crude residue was applied on a silica-gel column (CH$_2$Cl$_2$ to MeOH) to isolate **2** in good yield (60 mg, 0.143 mmol, 86.3%). ^{1}H-NMR (300 MHz, CD$_3$OD, p.p.m.) δ_H 4.16 (2H, q, -OCH$_2$CH$_3$), 3.58 (2H, m, BocNHCH$_2$), 3.22 (2H, m, CH$_2$), 1.94 (3H, s, -COCH$_3$), 1.79 (2H, m, CH$_2$), 1.63 (2H, m, CH$_2$), 1.44 (9H, s), 1.24 (3H, t, -OCH$_2$CH$_3$). Acidic hydrolysis of intermediate **2** (60 mg, 0.143 mmol) followed by Sep-Pak purification gave **L4** (41 mg, 0.127 mmol, 88.9%, calcd. for C$_7$H$_{19}$N$_6$O$_4$.2Cl). ^{1}H-NMR (300 MHz, D$_2$O, p.p.m.) δ_H 3.27 (2H, s, NH$_2$CH$_2$), 3.16 (2H, t, CH$_2$), 2.00–1.30 (4H, m, CH$_2$).^{13}C-NMR (75.5 MHz, D$_2$O, p.p.m.) δ_C 171.2 (CO), 157.3 (C, GuaNO$_2$), 61.2, 43.5, 36.8, 31.5, 22.3.ESI-MS (+) (m/z): 251.0 [M]$^+$; calcd for

$C_7H_{19}N_6O_4$ = 251.15. Retention time (analytical RP-HPLC, 220 nm): 5.7 min.

2-Amino-2-(aminomethyl)-6-(1-carboxy-4-(2-nitroguanidino)butylamino)-6-oxohexanoic acid (L5)

To a solution of **3** (87 mg, 0.224 mmol) in DMF was added O-benzotriazol-1-yl-*N*,*N*,*N*′,*N*′-tetramethyluronium hexafluorophosphate (HBTU, 101 mg, 0.268 mmol). After 10 min, N^{ω}-NO_2-L-arginine methyl ester (72 mg, 268 mmol) and NEt_3 (70 mg, 0.672 mmol) were also added. The reaction mixture was stirred at room temperature under nitrogen atmosphere for 2 h. The solvent was removed under vacuum and the residue purified by column chromatography ($CHCl_3$ to MeOH), yielding **5** as a colorless oil. Rf (silica-gel, CH_2Cl_2–MeOH 15%) = 0.40. Yield: 55.3% (75 mg, 0.124 mmol). ^{1}H-NMR (300 MHz, CD_3OD, p.p.m.) δ_H 4.45 (1H, m, Hα), 3.90 (2H, s, BocNHCH_2), 3.72 (3H, s, COOCH_3), 3.27 (4H, m, CH_2), 2.29 (2H, m, CH_2), 1.99 (3H, s, NHCOCH_3), 1.94 (2H, s, CH_2), 1.69 (4H, m broad, CH_2), 1.41 (9H, s, CH_3), 1.35 (9H, s, CH_3).^{13}C-NMR (75 MHz, CD_3OD, p.p.m.) δ_C 172.9 (CO), 171.5 (CO), 170.9 (CO), 159.7 (CO), 156.4 (C, GuaNO_2), 156.1 (CO), 83.7 (*C*(CH_3)), 79.9 (*C*(CH_3)), 65.2, 52.9 (CH_3), 51.3, 44.8, 40.6, 35.9, 32.0, 30.2, 29.8, 28.5 (C(CH_3)), 28.0 (C(CH_3)), 25.0, 24.1, 19.7, 18.6. Retention time (analytical RP-HPLC, 254 nm): 20.0 min. Compound **L5** was obtained directly from **5** (99 mg, 0.163 mmol) with a 2 M HCl solution (3 mL). After refluxing for 18 h, the solvent was evaporated to dryness and the oily residue obtained was thoroughly washed with CH_2Cl_2 and dried. After semi-preparative RP-HPLC purification, **L5** was obtained as colorless oil. Yield: 81.4% (78 mg, 0.132 mmol, calcd. for $C_{13}H_{25}N_7O_7\cdot$2TFA).^{1}H-NMR (300 MHz, D_2O, p.p.m.) δ_H4.24 (1H, m, Hα), 3.34 (2H, s, H_2NCH_2-), 3.13 (4H, m, CH_2), 2.29 (2H, t, CH_2), 1.93-1.40 (6H, m, CH_2). ^{13}C-NMR (75 MHz, D2O, p.p.m.) δ_C 173.2 (CO), 169.2 (CO), 168.9 (CO), 160.3 (q, CF_3COO^-), 156.3 (C, GuaNO_2), 113.5 (q, CF_3COO^-), 57.6, 49.9, 37.9, 37.7, 31.9, 30.4, 25.1, 24.4, 20.7, 16.3.ESI-MS (+) (m/z): 392.2 $[M+H]^+$, calcd. for $C_{13}H_{25}N_7O_7$ = 391.18. Retention time (analytical RP-HPLC, 220 nm): 8.5 min.

tert-*Butyl 2-acetamido-2-((tert-butoxycarbonylamino)methyl)-9-(1-methoxy-5-(2-nitroguanidino)-1-oxopentan-2-ylamino)-9-oxononanoate (6)*

Compound **6** was prepared using the same conditions described above for **5**. An excess of HBTU (58 mg, 0.153 mmol), N^{ω}-NO_2-L-arginine methyl ester (41 mg, 0.153 mmol) and NEt_3 (39 mg, 0.383 mmol) were added to **4** (55 mg, 0.130 mmol). Compound **6** was purified by column chromatography ($CHCl_3$ to MeOH) yielding a colorless oil. Rf (silica-gel, CH_2Cl_2–MeOH 15%) = 0.44. Yield: 71.5% (60 mg, 0.092 mmol). ^{1}H-NMR (300 MHz, $CDCl_3$, p.p.m.) δ_H 8.63 (1H, s, NH), 7.79 (2H, s, NH), 6.68 (2H, dd, NH), 4.88 (1H, s, Hα), 4.56 (1H, s, Hα), 3.69 (3H, s, COOCH_3), 3.55 (2H, m, CH_2), 3.27 (2H, m, CH_2), 2.19 (3H, m, CH_2 + CH), 1.95 (3H, s, NHCOCH_3), 1.87 (1H, s, CH), 1.55 (6H, m broad, CH_2), 1.41 (9H, s, CH_3), 1.35 (9H, s, CH_3), 1.19 (4H, m broad, CH_2). ^{13}C-NMR (75 MHz, $CDCl_3$, p.p.m.) δ_C 174.1 (CO), 172.7 (CO), 171.5 (CO), 170.1 (CO), 159.3 (CO), 155.7 (C, GuaNO_2), 82.9 (*C*(CH_3)), 79.3 (*C*(CH_3)), 65.1, 52.5 (CH_3), 50.7, 44.3, 40.3, 36.1, 32.1, 30.2, 29.6, 28.8, 28.2 (C(CH_3)), 27.6, 25.2, 25.1, 24.5, 23.9, 23.1, 23.0.

2-Amino-2-(aminomethyl)-9-(1-carboxy-4-(2-nitroguanidino)butylamino)-9-oxononanoic acid (L6)

Compound **L6** was obtained directly by hydrolysis of the protecting groups of **6** (55 mg, 0.128 mmol) with a 2 M HCl solution (3 mL) as previously described. After semi-preparative RP-HPLC purification, **L6** was obtained as a white solid. Yield: 23.6% (20 mg, 0.030 mmol, calcd. for $C_{16}H_{31}N_7O_7\cdot$2TFA). ^{1}H-NMR (300 MHz, D_2O, p.p.m.) δ_H 4.19 (1H, s, Hα), 3.27 (2H, m, H_2NCH_2-), 3.10 (2H, t, CH_2NH-C=NH_2), 2.11 (2H, t, CH_2CONH), 1.83-1.40 (8H, m, CH_2), 1.36-1.12 (6H, s broad, CH_2). ^{13}C-NMR (75 MHz, D_2O, p.p.m.) δ_C: 177.4 (CO), 175.5 (CO), 171.7 (CO), 162.8 (q, CF_3COO^-), 158.8 (C, GuaNO_2), 118.3 (q, CF_3COO^-), 67.4, 60.6, 52.2, 42.4, 40.5, 35.3, 33.3, 28.1, 27.7, 25.1, 23.0, 22.3. ESI-MS (+) (m/z): 434.1 $[M+H]^+$, calcd. for $C_{16}H_{31}N_7O_7$ = 433.2. Retention time (analytical RP-HPLC, 220 nm): 12.7 min.

Syntheses of Re4–Re6

Preparation of fac-[Re(CO)$_3$(κ^3-L)] (Re4, L = L4)

$[Re(CO)_3(H_2O)_3]Br$ (35 mg, 0.088 mmol) reacted with equimolar amounts of **L4**·2Cl (28 mg, 0.087 mmol) in refluxing water for 18 h. The solvent was removed under vacuum, and the resulting residue dissolved in water and purified by preparative RP-HPLC giving a colorless oil formulated as **Re4**. Yield: 35.2% (16 mg, 0.030 mmol, calcd. for $C_{10}H_{18}N_6O_7Re$). IR (KBr, cm^{-1}): 2020 and 1863 (C≡O), 1635 (C=O), 1596 (NO_2), 1279 (NO_2). ^{1}H-NMR (300 MHz, CD_3OD, p.p.m.) δ_H 5.32(1H, m, NH_2C), 4.95 (1H, NH_2C overlapped with H_2O peak; assigned from gCOSY spectrum),4.79 (1H, m, N$H_2$$CH_2$, 4.69 (1H, m, N$H_2$$CH_2$), 3.28 (2H, m, C$H_2$NH-C=N), 2.84 (1H, m, NH_2CH_2), 2.55 (1H, m, NH_2CH_2), 1.90- 1.59 (4H, m, CH_2).^{13}C-NMR (75.5 MHz, CD_3OD, p.p.m.) δ_c 197.2 (C≡O), 196.2 (C≡O), 179.9 (CO), 160.0 (C, GuaNO_2), 65.8, 45.6, 41.5, 31.2, 23.3. ESI-MS (+) (*m/z*): 543.0 $[M+Na]^+$; calcd for $C_{10}H_{18}N_6NaO_7Re$ = 544.0. Retention time (analytical RP-HPLC, 220 nm): 10.5 min.

Preparation of fac-[Re(CO)$_3$(κ^3-L)] (Re5, L = L5)

Compound **Re5** was synthesized and purified using the same conditions described above for **Re4**.

An excess of $[Re(CO)_3(H_2O)_3]Br$ (31 mg, 0.077 mmol) was reacted with **L5**·2TFA (40 mg, 0.064 mmol) in refluxing

H_2O for 18 h. **Re5** was isolated as a colorless oil. Yield: 75.7% (32 mg, 0.048 mmol, calcd. for $C_{16}H_{25}N_7O_{10}Re$). IR (KBr, cm^{-1}): 2010 and 1865 (C≡O), 1630 (C=O), 1590 (NO_2), 1270 (NO_2). ^{1}H-NMR (300 MHz, CD_3OD, p.p.m.) δ_H 5.31(1H, m, NH_2C), 4.92 (1H, NH_2C overlapped with H_2O peak; assigned from gCOSY spectrum), 4.80 (1H, m, N$H_2$$CH_2$),4.63 (1H, m, N$H_2$$CH_2$), 4.44 (1H, m, Hα), 3.28 (2H, m, CH_2NH-C=N), 2.79 (1H, m, $NH_2$$CH_2$), 2.55 (1H, m, $NH_2$$CH_2$),2.28 (2H, m, CH_2CONH), 1.90–1.59 (8H, m, CH_2).^{13}C-NMR (75.5 MHz, CD_3OD, p.p.m.) δ_c 197.0 (C≡O), 195.7 (C≡O), 180.2 (CO), 174.6 (CO), 173.9 (CO), 159.8 (C, GuaNO_2), 65.8, 51.9, 45.3, 40.5, 35.4, 33.4, 28.6, 25.0, 19.5. ESI-MS (-) (*m/z*): 660.1 [M-H]$^-$; calcd. for $C_{16}H_{25}N_7O_{10}Re$ = 561.6. Retention time (analytical RP-HPLC, 220 nm): 16.8 min.

Preparation of fac-[Re(CO)$_3$(κ^3-L)] (Re6, L = L6)

Compound **Re6** was synthesized and purified using the same conditions described above for **Re4**. [Re(CO)$_3$(H_2O)$_3$] Br (10 mg, 0.023 mmol) reacted with equimolar amounts of **L6**·2TFA (15 mg, 0.023 mmol) in refluxing H_2O for 18 h. **Re6** was isolated as a colorless oil. Yield: 74.1% (12 mg, 0.017 mmol, calcd. for $C_{19}H_{31}N_7O_{10}Re$). ^{1}H-NMR (300 MHz, CD_3OD, p.p.m.) δ_H 5.21 (1H, m, NH_2C), 4.90 (1H, NH_2C overlapped with H_2O peak; assigned from gCOSY spectrum), 4.70 (1H, m, N$H_2$$CH_2$, 4.60 (1H, m, N$H_2$$CH_2$), 4.39 (H, m, Hα), 3.20 (2H, m, CH_2NH-C=N), 2.75 (1H, m, $NH_2$$CH_2$), 2.55 (1H, m, $NH_2$$CH_2$), 2.25 (2H, m, CH_2CONH), 1.91–1.3 (14H, m, CH_2). ^{13}C NMR (75 MHz, CD_3OD, p.p.m.) δ_C 196.9 (CO), 181.5 (CO), 176.4 (CO), 175.2 (C), 160.0 (C, GuaNO_2), 67.3, 53.1, 46.8, 41.7, 36.6, 35.2, 31.0, 30.6, 29.6, 26.7, 24.0, 19.5. ESI-MS (-) (*m/z*): 702.2 [M-H]$^-$; calcd. for $C_{19}H_{31}N_7O_{10}Re$ = 703.1. Retention time (analytical RP-HPLC, 220 nm): 18.5 min.

Syntheses of the ^{99m}Tc(I) complexes fac-[^{99m}Tc(CO)$_3$(κ^3-L4)] – fac-[^{99m}Tc(CO)$_3$(κ^3-L6)] (Tc4–Tc6)

General method

In a nitrogen-purged glass vial, 100 μL of an aqueous solution of the compounds (**L4**–**L6**; 10^{-4} M) was added to 900 μL of a solution of the organometallic precursor fac-[^{99m}Tc(H_2O)$_3$(CO)$_3$]$^+$ (1–2 mCi) in saline (pH 7.4), which was prepared using an IsoLink kit (Mallinckrodt, Covidien). The reaction mixture was heated to 100 °C for 30 min, cooled in a water bath, and analyzed by RP-HPLC (γ detection). Retention times: 10.1 min (**Tc4**), 16.3 min (**Tc5**), and 18.9 min (**Tc6**).

Enzyme kinetic assays

The iNOS activity assay was based on the method of hemoglobin assay previously described with slight modifications (26,27). The kinetic parameters for iNOS were determined using initial rate analysis. Initial rate data were fitted to irreversible single substrate Michaelis-Menten models. The kinetic parameters were determined using the direct linear plot of Eisenthal and Cornish-Bowden and the HYPER software (J.S. Easterby, University of Liverpool, UK; http://www.liv.ac.uk/~jse/software.html).(28, 29) The K_i values represent a mean of triplicate measurements. Standard deviations of ±5 to 10% were observed.

Hemoglobin capture assay

Preparation of Oxyhemoglobin

Oxyhemoglobin was prepared using a previously described protocol with some modifications (28). Briefly, bovine hemoglobin in 50 mM HEPES pH 7.4 was reduced to oxyhemoglobin with tenfold molar excess of sodium dithionite. The sodium dithionite was later removed by dialysis against 50 volumes of HEPES buffer for 18 h at 4 °C. The buffer was replaced three times. The concentration of oxyhemoglobin was determined spectrophotometrically using $\varepsilon_{415\ \text{nm}} = 131$ mM^{-1} cm^{-1}. Oxyhemoglobin was stored at −80 °C before use.

Determination of K$_i$ values

All initial velocity measurements were recorded at 37°C. Total reaction volumes were 600 μL and contained 50 mM HEPES pH 7.4, 6 μM oxyhemoglobin, 200 μM NADPH, 10 μM BH_4, 100 μM DTT, and at least three concentrations of L-arginine (20–150 μM) in the presence of 150 μM of the inhibitor. Reactions were initiated by the addition of iNOS enzyme (~1 U) to the prewarmed cuvette (~5 min). The NO-mediated conversion of oxyhemoglobin to methemoglobin was followed by monitoring the increase in absorbance at dual wavelength (401 and 421 nm) for 10 min. Controls were performed in the same conditions without iNOS enzyme. The formula used to calculate the K_i is: $K_i = [I]/((K_m^{app}/K_m) - 1)$, where [I] is the inhibitor concentration, K_m is the Michaelis-Menten constant of the substrate L-arginine, and K_m^{app} is the apparent value of K_m for a substrate in the presence of the inhibitor (29). K_m value for L-arginine was determined as 6 μM.

RAW 264.7 macrophages assay

Cell culture. RAW 264.7 macrophages were grown in Dulbecco's modified Eagle medium (DMEM) with GlutaMax I supplemented with 10% heat-inactivated fetal bovine serum and 1% penicillin/streptomycin antibiotic solution (all from Gibco, Alfagene, Lisbon). Cells were cultured in a humidified atmosphere of 95% air and 5% CO_2 at 37 °C, with the medium changed every other day. The cells were adherent in monolayers and, when confluent, were harvested from the cell culture flasks, using a scrapper, and seeded farther apart.

Evaluation of the inhibitory effect of compounds L4–L6 and Re4–Re6 in NO biosynthesis in LPS-activated RAW 264.7 macrophages. Macrophages (in DMEM without phenol red and 10% FBS) were plated at a density of 9×10^4 cells per well in 96-well plates. Cells were immediately induced with 10 μL of LPS (2 μg/mL in PBS) for 4 h and then incubated for 24 h in the presence of various concentrations of compounds (total volume 200 μL). At the end of the incubation period, the culture medium was collected and assayed for nitrite production using the commercially available Griess reagent method (Sigma-Aldrich, St Louis, MO, USA) (30).

Cytotoxic activity

Cytotoxic activity was evaluated by the MTT assay (MTT = 3-(4,5-dimethylthiazol-2-yl)-2,5-diphenyltetrazolium bromide) (31). RAW 264.7 macrophages were plated in 96-well sterile plates at a density of 9×10^4 cells per well, incubated for 4 h with LPS, and then incubated for more 24 h in the presence of various concentrations of compounds. At the end of the incubation period, the compounds were removed and cells were incubated with 200 μL of MTT solution (0.5 mg/mL). After 3–4 h at 37 °C/5% CO_2, the medium was removed and the purple formazan crystals formed inside the cells were dissolved in 200 μL DMSO by thorough shaking. The cellular viability was evaluated by measurement of the absorbance at 570 nm using a plate spectrophotometer (PowerWaveXs, Bio-Tek Instruments, Winooski, VT, USA). The viability of cells in the presence of the tested compounds was compared to that observed in control cultures. All compounds were tested in at least two independent studies with six replicates.

Computational studies

Docking calculations

AutoDock 4.2 was employed to perform protein–ligand docking calculations. The protein structure used in the docking studies were taken from the Research Collaboratory for Structural Bioinformatics (RCSB) protein database (pdb id code 1QW4) (32). A property of the AUTODOCK software is its ability to take into account the flexibility of the enzyme during docking process. According to the literature, the most important residues of the iNOS enzyme for catalytic activity were considered fully flexible during the docking process (Gln257, Tyr341, Trp366, Tyr367, and Glu371 residues; Figure S1) (33,34). The rotatable bonds and the atomic partial charges (Gasteiger) were assigned using AUTODOCK tools. The protein–ligand complexes were prepared with AutoDock Tools: For the protein, hydrogen atoms were added and Kollman united atom charges were assigned. Hydrogens were also added to the ligands, heme and H_4B, and charges were calculated by the Gasteiger-Marsili method. A charge of +3 was assigned for the Fe atom of the heme group. The ligands were docked inside a cubic grid box (48 × 32 × 58 Å) centered on the Fe atom of the heme group with a grid spacing of 0.375 Å. In each docking simulation, 100 independent Lamarckian genetic algorithm (LGA) runs were performed, with the population size set to 200, the number of energy evaluations set to 10 000 000, and the maximum number of generations set to 27 000. All other parameters were maintained at their default settings (35,36). The resulting docked conformations within a RMSD of 2 Å were clustered together. The lowest and more populated energy cluster returned by AUTODOCK that fulfilled some known structural criteria important for enzyme activity was used for conformational binding analysis.

The protonation state of the inhibitors at physiological pH was determined with Epik 1.6 (Schrödinger) (37). All rotatable bonds of **L4** were kept free. In the case of **L5** and **L6,** all rotatable bonds were kept free with exception of the rotatable bonds of the N^{ω}-NO_2-L-Arg moiety, which was kept rigid in the same conformation found on the X-ray structure of this inhibitor complexed with nNOS (pdb id 1K2R) (Figure S17) (38). In the case of **Re4–Re6,** the 3D structure information of the dap chelating unit, which stabilizes the *fac*-$[Re(CO)_3]^+$ core, was taken from the Cambridge Crystallographic Data Centre (reference number CCDC 761462) (17). The docking experiments were carried out allowing **Re4–Re6** to rotate freely with exception of the rotatable bonds of the dap chelating unit and the N^{ω}-NO_2-L-Arg moiety (Figure S17), which were kept in the conformation found in the X-ray structures. A charge of 0 was assigned for the rhenium atom of **Re4–Re6**. The complexes **L4**:iNOS, **L5**:iNOS, **L6**:iNOS, **Re4**:iNOS, **Re5**: iNOS, and **Re6**:iNOS chosen after analyses of the docking results were subjected to molecular dynamics (MD) simulations.

Molecular dynamics simulations

DFT calculations have been shown to give very accurate results for systems involving transition metals (39). Among the plethora of existing density functional, we chose the B3LYP which has been shown to be an appropriate choice for transition metal complexes and rhenium specifically (40–44). The geometries of the inhibitors **L4–L6** and **Re4–Re6** were optimized using the B3LYP/6-31G* level of theory with the Gaussian 09 program (version A.02), whereas charge fitting was performed using the RESP program (45,46). The molecular electrostatic potential (MEP) computation was carried out using the same level of theory and the Connolly surface algorithm (47). In the case of the rhenium complexes, it was used the B3LYP level of theory with the 6-31G* basis set for all atoms and the SDD basis set for rhenium. The SDD basis set uses the small core quasi-relativistic Stuttgart/Dresden electron core potentials for transition elements (48–50). A spin multiplicity of 1, a charge of 0, and a radius of 1.47 Å for Re(I) were considered in the DFT calculations. The charge derivation procedure was automatically carried out using the R.E.D. (RESP ESP charge Derive) Server version 2.0 (51–53). A detailed description of this procedure is reported in the Supporting Information section (Figure S18).

The topologies and parameters of the organic molecules (**L4**–**L6**) compatible with the CHARMM all atoms force field were derived from the ParamChem server (https://www.paramchem.org/).(44) Parameters for the metal fragment were taken from previous parameterization studies of technetium and rhenium complexes (54–63). All the dihedral parameters involving the Re–ligand interactions were set to zero. This procedure has been used with success in the treatment of several different systems that have a metal atom covalently bonded (64–66). Lennard–Jones parameters are also not parameterized due to the fact that the rhenium metal is buried and that van der Waals interactions are not as important as the electrostatics (67). Lennard–Jones parameters for the metal were taken from the literature (60).

Based on the docking results, MD simulations for compounds **L4**–**L6** and **Re4**–**Re6** were performed using NAMD(68) and CHARMM22 force field (69). The iNOS isoform exists as dimer with a structural Zn^{2+} ion co-ordinated by four cysteines, two cysteines from each monomer (Cys104 and Cys109). Aiming to avoid the challenging task of parameterization of the Zn^{2+} ion, which was shown to be 22 Å away from the bound site and have no effect on the ligand binding, it was excluded from the simulation. To increase length of the simulations without losing important structural information, only one oxygenase monomer was selected. As the H_4B cofactor is placed at the dimer interface by interactions with both monomers, light constraints were needed to fix this cofactor to its crystallographic position (34).

The oxo-ferryl form (compound I) of heme, which has an oxygen atom at the sixth co-ordination position of iron, was used. The force field parameters of the H_4B cofactor and compound I were kindly provided by Cho *et al.* (70). The propKa module of the PDB2PQR server (http://kryptonite.nbcr.net/pdb2pqr/) was used to adjust the protonation states of ionizable residues at physiological pH (71–73). Water molecules observed in the crystal structure were kept, and additional TIP3P water molecules (box of dimension 10 Å × 10 Å × 10 Å) were modeled using the solvate package in Visual Molecular Dynamics (VMD) (74). Next, the systems were neutralized by adding counter ions with the autoionize package in VMD. The whole systems contained the following: **L4**:iNOS—418 residues, 17072 water molecules, and 4 Na^+ (58096 atoms in total); **L5**: iNOS—418 residues, 17067 water molecules, and 5 Na^+ (58100 atoms in total); **L6**:iNOS—418 residues, 17068 water molecules, and 3 Na^+ (58109 atoms in total); **Re4**: NOS—418 residues, 17072 water molecules, and 1 Na^+ (58097 atoms in total); **Re5**:NOS—418 residues, 17073 water molecules, and 1 Na^+ (58119 atoms in total); and **Re6**:NOS—418 residues, 17069 water molecules, and 1 Na^+ (58116 atoms in total).

All models were subjected to 3000 energy minimization steps (6 ps), and then MD continued for another 8 ns in 2 fs time steps. Covalent bonds involving hydrogen atoms were constrained to their equilibrium length. The force field parameters were kept standard as specified by the charm force field. Short-range non-bonded van der Waals interactions were computed every 2 fs, and the long-range electrostatic ones were computed every 4 fs. Starting from a switching distance of 1 nm, the Lennard-Jones potential was smoothly reduced to zero at a cutoff distance of 1.2 nm. The particle mesh Ewald (PME) algorithm with a grid spacing of 1 Å was used for electrostatics (75). The target temperature was 310 K in all simulations. This was controlled using Langevin dynamics with the friction coefficient set to 5 ps (76). The pair list of the non-bonded interaction was recalculated for every ten time steps with a pair list distance of 16.0 Å. In NPT simulations (constant pressure, particle number, and temperature), pressure was controlled using the modified Langevin piston Nosé-Hoover method with a barostat oscillation coefficient of 200 fs and a damping coefficient of 50 fs (77–79). The anisotropic pressure coupling scheme was used in the NPT simulations. Target pressure was 1 atm.

The geometric parameters (bonds and angles) of the rhenium complexes from the simulation were examined. All distances and angles confirm the experimental X-ray structure, having only a small fluctuation (around 0.3–0.4 Å for distances and 1–2° for angles).

VMD version 1.8.7 was used for trajectory analysis (74). Several detailed analyses were carried out for the trajectories obtained from the last 3 ns of the equilibrated simulations. The averaged structures of the last 3 ns of the simulations were also calculated using appropriate in-house scripts. The hydrogen bond analysis was performed using the HBOND routine in VMD using a distance cutoff of 3.5 Å and an angle cutoff of 30°. All pictures were made with the PYMOL software (80).

Results and Discussion

Synthesis and characterization of the conjugates L4–L6 and $M(CO)_3$ complexes Tc4/Re4–Tc6/Re6

Conjugates **L4**–**L6**, which contain the dap chelating unit and pendant propyl-NO_2-guanidino (**L4**) or N^{ω}-NO_2-L-arginine moieties (**L5** and **L6**), were synthesized as depicted in Scheme 1. **L4** was prepared by conversion of the primary amine of the previously described precursor **1** into a NO_2-guanidino group upon reaction with the guanylating agent 2-methyl-1-nitro-2-thiopseudourea, followed by full deprotection of the resulting compound under acidic conditions (17).

L5 and **L6** were synthesized in a two-step procedure by direct conjugation of precursors **3** and **4**, respectively, to N^{ω}-NO_2-L-arginine methyl ester using standard coupling reagents, followed by deprotection under acidic conditions. The novel precursor **4** has been synthesized

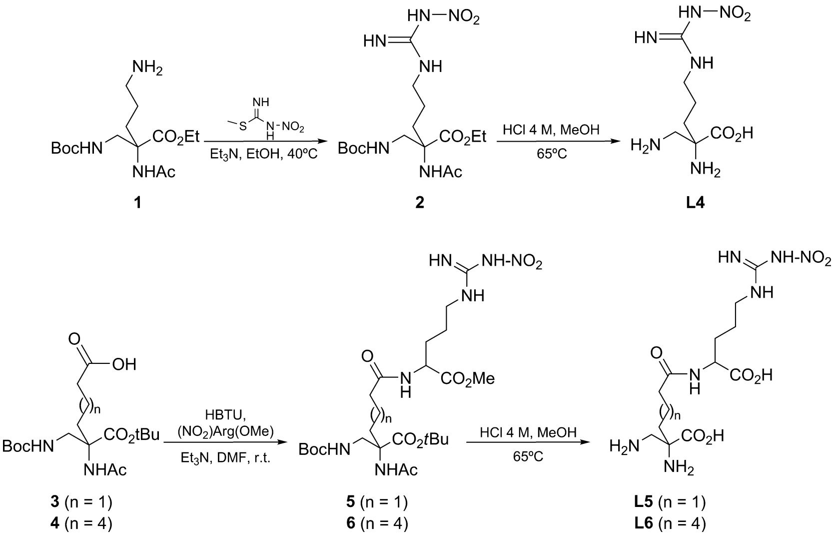

Scheme 1: Synthesis of conjugates **L4**–**L6**.

following a synthetic procedure similar to the one for compound **3** (Scheme S1, Supporting Information) (17). All compounds were fully characterized by ^{1}H/^{13}C-NMR spectroscopy (including 2D NMR experiments such as ^{1}H-^{1}H COSY and ^{1}H-^{13}C HSQC) and electrospray ionization mass spectrometry (ESI-MS).

The neutral organometallic complexes of the type *fac*-[^{99m}Tc(CO)$_3$(κ^3-L)] (**Tc4**, L = **L4**; **Tc5**, L = **L5**; **Tc6**, L = **L6**) were prepared in high radiochemical yield (>95%) and radiochemical purity (>95%) upon the reaction of **L4**–**L6** with the precursor *fac*-[^{99m}Tc(CO)$_3$(H$_2$O)$_3$]$^+$ (Scheme 2). The latter was prepared by the addition of Na[^{99m}TcO$_4$] in saline, eluted from a ^{99}Mo/^{99m}Tc generator, to an IsoLink kit (Mallinckrodt, Covidien) and heating (95 °C) for 20 min (Scheme 2). The kit formulation, available for research purposes, contains boranocarbonate ([H$_3$BCO$_2$]$^{2-}$), Na/K tartrate, sodium tetraborate decahydrate, and sodium carbonate. The boranocarbonate reduces Tc(VII) to Tc(I) and acts simultaneously as a CO source, through a mechanism not yet fully understood (81).

The high stability of the complexes was demonstrated by incubating **Tc4**–**Tc6** with a hundredfold excess of co-ordinating amino acids such as histidine or cysteine; no degradation or transchelation occurred under these conditions (37 °C, samples collected and analyzed up to 6 h by RP-HPLC), in line with earlier results obtained with other complexes stabilized through the same chelating unit (17,19,20).

The dilute nature of the solutions of the ^{99m}Tc complexes (ca. 10^{-8}–10^{-10} M) hampers their structural characterization by the usual analytical methods in chemistry (e.g., NMR and IR spectroscopy). The simplest way to overcome this issue is to compare the chromatographic behavior of the ^{99m}Tc complexes with that of the corresponding compounds prepared at the 'macroscopic' scale with natural rhenium. Indeed, technetium and rhenium, transition metals of group 7 of the periodic table, share similar co-ordination chemistry, and, consequently, rhenium complexes can be used as non-radioactive ('cold') surrogates of the respective ^{99m}Tc complexes.

It is worth mentioning that comparison of HPLC retention times of rhenium and ^{99m}Tc homologues for identifying the structure of the latter ones is a FDA-accepted procedure in radiochemistry (82).

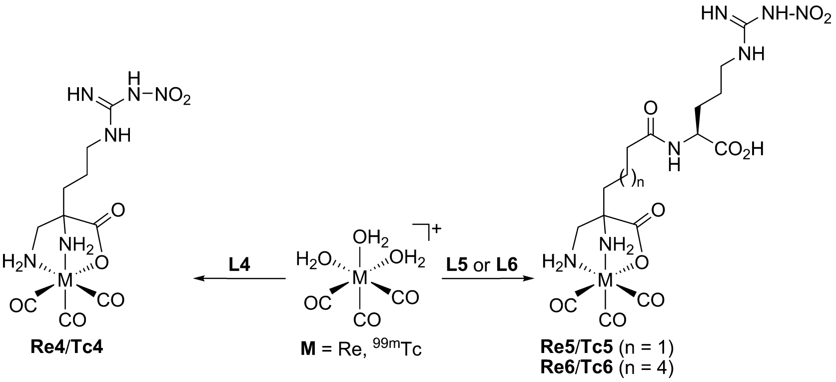

Scheme 2: Synthesis of complexes of the type *fac*-[M(CO)$_3$(κ^3-L)] (M = Re/^{99m}Tc, L = **L4**–**L6**).

Therefore, the chemical identity of the ^{99m}Tc(I) complexes **Tc4**–**Tc6** was established by comparing their RP-HPLC analytical radioactive traces (γ detection) with the UV-Vis traces of the surrogate complexes **Re4**–**Re6**. The latter were prepared by reacting **L4**–**L6** with *fac*-[Re$(CO)_3(H_2O)_3]^+$ in refluxing water (Scheme 2). The complexes were obtained in moderate to high yields (35–75%) after evaporation of the reaction solvent and purification by semi-preparative RP-HPLC (>95% purity).

The rhenium compounds were fully characterized by ESI-MS, IR, and NMR spectroscopy (^{1}H/^{13}C NMR, ^{1}H-^{1}H COSY, and ^{1}H-^{13}C HSQC). Brought together, the spectral data obtained support well the proposed structure for the complexes and the tridentate co-ordination mode of the dap containing conjugates, comparing well with the similar complexes previously described (17).

Enzymatic Assays with purified iNOS

The conjugates **L4**–**L6** and the respective rhenium complexes (**Re4**–**Re6**) were tested as competitive inhibitors of purified mouse recombinant iNOS. The activity of the enzyme was determined spectrophotometrically by monitoring the NO-mediated conversion of oxyhemoglobin to methemoglobin at 401 and 421 nm. The kinetic parameter K_i for each compound under study was determined by the method of Eisenthal and Cornish-Bowden, and the results are summarized in Table 1 (26,27,83).

Although the inhibitory potency of conjugates **L4** (K_i = 29.4 μM) and **L6** (K_i = 759.6 μM) is lower than that observed for the free non-conjugated inhibitor N^{ω}-NO_2-L-arginine (K_i = 3–8 μM), the potency of **L5** (K_i ~ 6 μM) is comparable to that of the non-conjugated inhibitor, demonstrating that in this case conjugation of the inhibitor to the dap-based chelator did not affect its inhibitory potency.

Table 1: K_i values for iNOS Inhibitors **L1**–**L6** and **Re1**–**Re6**

Compound	K_i value (μM)^a
N^{ω}-NO_2-L-arginine	3.0 ± 1.0 (87)
L1	1087.9 ± 183.0 (15, 16)
Re1	257.3 ± 52.9 (15, 16)
L2	178.1 ± 10.7 (15, 16)
Re2	84.1 ± 6.5 (15, 16)
L3	36.0 ± 3.7 (15, 16)
Re3	6.2 ± 2.5 (15, 16)
L4	29.4 ± 3.3
Re4	240.6 ± 4.6
L5	6.2 ± 1.6
Re5	57.2 ± 8.4
L6	759.6 ± 13.6
Re6	258.7 ± 5.7

^{a}Results are given as a mean of three or more independent experiments.

Unlike the N^{ω}-NO_2-L-arginine containing conjugates **L1**–**L3** with the pyrazolyl-diamine chelating unit, which upon metallation with *fac*-[Re$(CO)_3]^+$ led to complexes with higher inhibitory potency (**Re1**–**Re3**), conjugates **L4** (K_i = 29.4 μM) and **L5** (K_i = 6.2 μM) gave complexes that are eightfold (**Re4**, K_i = 240.6 μM) and ninefold (**Re5**, K_i = 57.2 μM) less potent than the respective free conjugates. The only exception is the match pair **L6**/**Re6**, in which the inhibitory potency of **L6** increased moderately after metallation, following the trend previously observed for the match pairs **L1**/**Re1**, **L2**/**Re2,** and **L3**/**Re3**.

Nevertheless, the dap containing complexes **Re4** (K_i = 240.6 μM) and **Re5** (K_i = 57.2 μM) present inhibitory potencies comparable to those of the congeners **Re1** (K_i = 257.3 μM) and **Re2** (K_i = 84.1 μM), which present a pyrazolyl-diamine chelating framework. This result is assigned to the presence of a similar iNOS-recognizing moiety (Figure 1 and Scheme 2). Comparing **Re3** and **Re6**, which have the same iNOS-recognizing moiety but different chelating units, complex **Re6** (K_i = 258.7 μM) has 46-fold less potency than the previously described complex **Re3** (K_i = 6.2 μM).

Assay of iNOS activity in LPS-treated murine RAW 264.7 macrophages

The ability of **L4**–**L6** and respective rhenium complexes **Re4**–**Re6** to inhibit intracellular iNOS was assessed in LPS-activated murine RAW 264.7 macrophages, which produce high levels of NO due to iNOS overexpression, checked by Western blot analysis of protein extracts using an anti-iNOS antibody (15). The assay evaluated the ability of the compounds to suppress NO biosynthesis by measuring nitrite accumulation in the culture media using the Griess reagent method (Figure 2) (30). Additionally, aiming to assess the

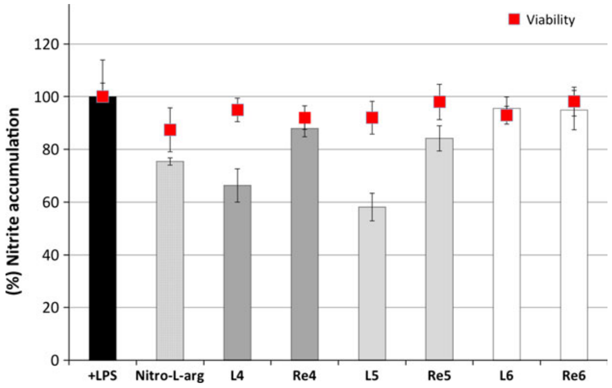

Figure 2: Effect of compounds **L4**–**L6** and **Re4**–**Re6** in nitrite accumulation and cell viability in lipopolysaccharide (LPS)-induced RAW 264.7 macrophages (mean ± SD, n = 8). Final concentration of all compounds was 500 μM. NO production and viability in LPS-induced cells in the absence of any compound (control) was considered 100%. This experiment was repeated twice with comparable results.

intrinsic cytotoxicity of the compounds at the concentration used in the NO assay (500 μM), a cell viability study (MTT assay) was also performed in parallel (31). The results evidenced that all compounds are non-toxic under the described experimental conditions (Figure 2).

The NO assay demonstrated that **L4** (ca. 33% inhibition) and **L5** (ca. 41% inhibition) displayed a significantly higher inhibitory potency toward NO biosynthesis by LPS-activated macrophages than the respective metallated analogues **Re4** (ca. 10% inhibition) and **Re5** (ca. 15% inhibition). Remarkably, **L4** presented an inhibitory potency comparable to that of the non-conjugated inhibitor N^{ω}-NO_2-L-arginine (ca. 25% inhibition), whereas **L5** inhibited NO biosynthesis in a more effective way than N^{ω}-NO_2-L-arginine. This assay confirmed also that **L6** and **Re6** presented negligible inhibitory potency toward iNOS. Brought together, the results obtained in the cell assay with LPS-activated macrophages corroborate the main conclusions drawn from the *in vitro* enzymatic assays performed with purified iNOS. Indeed, **L4** and **L5** exhibited the highest inhibitory potency toward iNOS biosynthesis.

Aiming to attain a structural understanding of the possible rearrangements between the conjugates (**L4**–**L6**) and the respective rhenium complexes (**Re4**–**Re6**) within the binding site of iNOS that could justify the different enzymatic properties already mentioned, we applied a combined approach of molecular docking and molecular dynamics (MD) simulations.

Modeling of the compounds in the active site of iNOS

We used the AUTODOCK software to dock **L4**–**L6** and **Re4**–**Re6** into the iNOS isoform. According to our recent studies, the most important residues in the active pocket of iNOS for catalytic activity are Gln257, Tyr341, Trp366, Tyr367, and Glu371 (33). These residues seem to give an important contribution for the stabilization of L-arginine derivatives, as is the case of **L4**–**L6** and **Re4**–**Re6**, and they were considered fully flexible during the docking process (Figure S1). Figure S2 illustrates the complex docking decoys with the best scoring energies. The top 10 lowest energy conformations obtained by docking are also depicted in Figures S3–S8.

With the goal of investigating the conformational changes of the compounds relative to the active pocket and study the binding stability, we performed MD simulations of the above-mentioned docking structures. The MD simulations predicted the formation of stable systems for all the compounds in complex with iNOS (Figure S9–S12). The backbone root-mean-square deviation (RMSD) values reached a stable plateau around 1.5–2.8 Å after 3 ns. For the sake of example, the RMSD values for the systems **Re4**:iNOS, **Re5**:iNOS, and **Re6**:iNOS are shown in Figure S9.

Analysis of the MD trajectories—overall interactions

Residue Glu371 in the active pocket is known to be responsible for positioning the inhibitor analogues of L-arginine over the heme group (33). Therefore, a reliable model should maintain a reasonable distance between the nitrogen atoms Nε and Nη1 of the NO_2-guanidine moiety in the compounds (**L4**–**L6** and **Re4**–**Re6**) and Glu371. The MD simulations suggest that in all cases, the N^{ω}-NO_2-guanidine moiety occupied the expected binding site, being stable throughout the simulation (Figure S10 and S11). The H-bonds observed between Glu371 and the nitrogen atoms Nε and Nη1 of the NO_2-guanidine moiety are relatively short (d (Nη1····OE1) = 2.65–3.30 Å and d(Nε····OE2) = 2.59–4.32 Å, Table S1) and are comparable with the experimental data (d(Nη1····OE1) = 2.95 Å and d(Nε····OE2) = 3.01Å from pdb id 1K2R, N^{ω}-NO_2-L-Arg:iNOS). The position of N^{ω}-NO_2-L-Arg seems to be unaffected by conjugation to the dap chelator through its α-amino group. The predicted binding modes of **L4**–**L6** and **Re4**–**Re6** are shown in Figure 3.

The high affinity of **L4** (K_i = 29.4 μM) and **L5** (K_i = 6.2 μM) for the enzyme is probably due to the stronger interactions observed between the NH_3^+ and CO_2^- groups of the dap chelating unit and polar residues of iNOS, such as Gln257, Arg260, Tyr341, and Asp376 (Figure 3A,B). The inhibitory potency of **L5** (K_i = 6 μM) is comparable to that of the free non-conjugated inhibitor N^{ω}-NO_2-L-Arg (K_i = 3 μM) and five-fold higher than that observed for **L4**. The MD simulations suggest that the flexible spacer of **L5** improves the ability of the dap chelating unit to be accommodated near the heme carboxylate arms, thus enhancing the interaction of **L5** through the formation of stronger H-bonds between the terminal protonated amines of the dap and the CO_2^- groups of the heme propionates A and D (Figure 3B). In the case of **L5** and **L6,** the MD simulations showed that the interactions among the N^{ω}-NO_2-L-Arg moieties and the residues of the binding cavity (Gln257, Arg260, Tyr341, and Glu371) are very similar (Figure 3B,C). However, the overall conformation is distinct due to the different positions of the dap chelator of **L5** (K_i = 6.2 μM) and **L6** (K_i = 759.6 μM). Indeed, in **L6** the dap chelator is stabilized mainly by interactions with the residues Asn115 and Asn348 (Figure 3C), instead of the heme propionates A and D as observed for **L5** (Figure 3B). A complete analysis of the H-bonds formed between **L5**/**L6** and the enzyme seems to indicate that the **L5**:iNOS complex has an higher occupancy of stable H-bonds (Figure S13 and Table S2). As water molecules can play an important role in ligand binding, water-mediated interactions between **L5**/**L6** and iNOS were also monitored during the simulation. This analysis seems to indicate that **L5**:iNOS engages a higher number of water molecules in the interface inhibitor:protein, mediating the formation of H-bonds with the residues of the active site and therefore possessing higher affinity (Figure S14, 9 water molecules for **L5** versus 6 water molecules for **L6** with residence times of 100% for the last 3 ns). Based on the H-bonding network and water pattern distribution, **L5** is envisaged to have

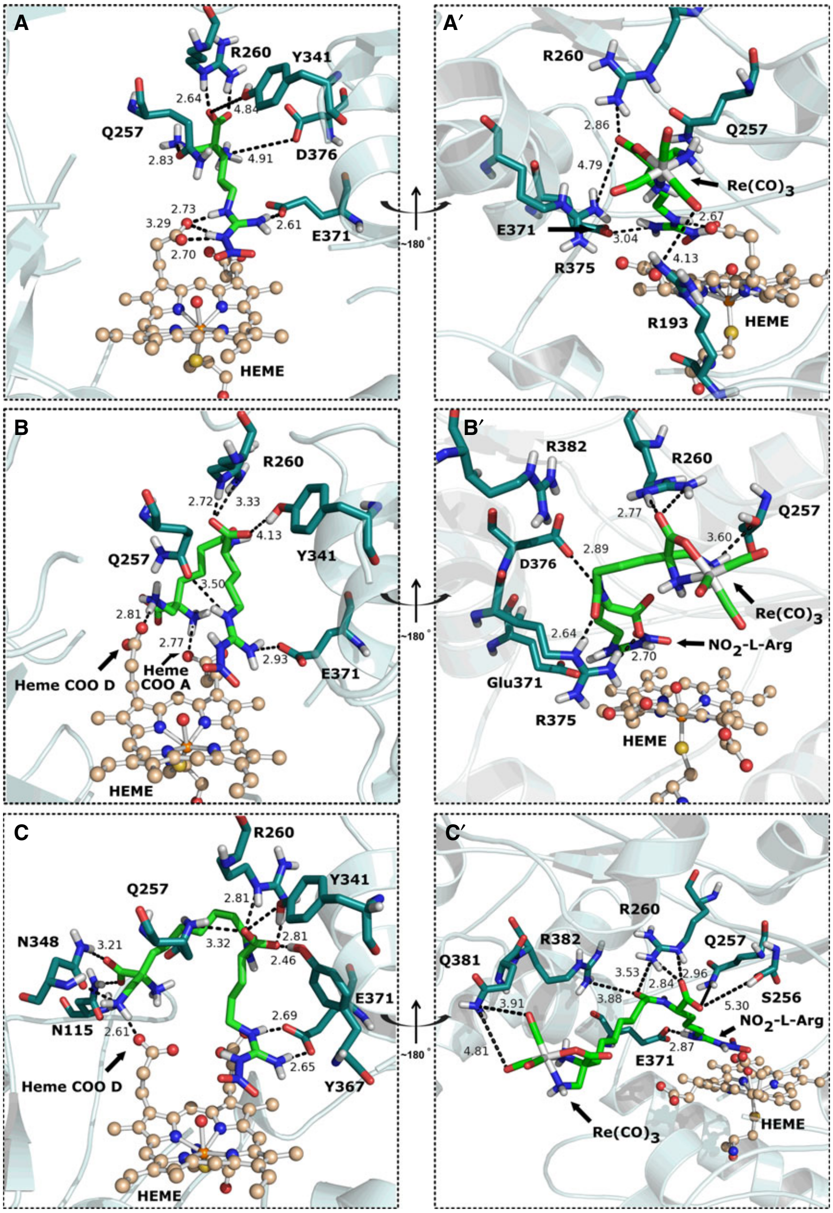

Figure 3: Averaged structures of the compounds in the active site calculated over the last 4 ns of the MD simulation: **L4**(**A**), **Re4**(**A′**), **L5**(**B**), **Re5**(**B′**), **L6**(**C**), and **Re6**(**C′**). Selected active site residues important for the stabilization of **L4**–**L6** and **Re4**–**Re6** are shown in blue sticks. Dashed lines showed distances in Å between atoms.

higher binding affinity compared to **L6**. However, there is another contribution for the difference in affinity between these ligands, which comes from the entropy penalty associated with the additional 3 single bonds and 3 additional buried water molecules in the complex **L5**:iNOS that cannot be easily estimated.

As described before, metallation of **L4** and **L5** led to complexes with lower affinity, which can be most likely assigned to the loss of the strong interactions previously described for the systems **L4**:iNOS and **L5**:iNOS. Indeed, after coordination to the *fac*-$[\mathrm{Re(CO)_3}]^+$ core, the $\mathrm{NH_3}^+$ and $\mathrm{CO_2^-}$ groups of the dap chelating unit are no longer available to interact with the heme carboxylate arms and other polar residues (e.g., Gln257, Arg260, Asp376) (Figure 3A′ and 3B′). The organometallic tails of complexes **Re4** and **Re5** showed contacts with Arg260, Arg275, Ser256, and Gln257 residues situated near the heme binding pocket.

The enzymatic assays showed that **Re5** (K_i = 57 μM) exhibited the highest inhibitory potency when compared to **Re4** (K_i = 240 μM) and **Re6** (K_i = 258 μM). This finding could be explained based on the relatively higher bulkiness of the organometallic tail of **Re5**, which provides a more extensive contact surface area than the smaller organometallic tail of **Re4**. Moreover, the absence of strong anchoring interactions in **Re4**, for example, the $\mathrm{CO_2^-}$ group of the $\mathrm{N^{\omega}}$-$\mathrm{NO_2}$-L-Arg moiety present in **Re5**, also should contribute for the fourfold lower affinity toward iNOS (Figure 3A′ and 3B′).

Finally, the striking difference in the inhibitory potency observed for complexes **Re6** (K_i = 258.7 μM) and **Re3**

($K_\mathrm{i} = 6.2\ \mu\mathrm{M}$), which share the common NOS-recognizing unit but are stabilized by chelators of different nature (**Re6**: dap based; **Re3**: pyrazolyl-diamine based), can be rationalized in terms of the different position of the *fac*-$[\mathrm{Re(CO)_3}]^+$ organometallic moiety. In **Re6**, the bulky organometallic moiety is less accommodated inside the active pocket of iNOS as it is oriented toward its 'open entrance' (Figure 3C′ and Figure S15). Such orientation is triggered by electrostatic repulsions observed between the $\mathrm{CO_2^-}$ group of dap-$\mathrm{Re(CO)_3}$ and the heme carboxylate group (Figure S15). This results in a smaller number of contacts between the Re complex and the enzyme, mainly the strong electrostatic contacts observed between the *fac*-$[\mathrm{Re(CO)_3}]^+$ core of **Re3** and the residues Arg260 and Arg382 in iNOS (Figure S16) (34).

Conclusions

We have introduced conjugates comprising a 2,3-diaminopropionic acid chelating unit and $\mathrm{NO_2}$-guanidine (**L4**) or N^ω-$\mathrm{NO_2}$-L-arginine (**L5** and **L6**) groups as nitric oxide synthase recognizing moieties. The conjugates **L4**–**L6** reacted with *fac*-$[\mathrm{Re(CO)_3(H_2O)_3}]^+$ yielding compounds of the type *fac*-$[\mathrm{Re(CO)_3}(\kappa^3\text{-L})]$ (**Re4**, L = L4; **Re5**, L = L5; **Re6**, L = **L6**). The enzymatic assays with murine-purified iNOS have shown that unlike the N^ω-$\mathrm{NO_2}$-L-arginine-containing conjugates **L1**–**L3** with the pyrazolyl-diamine chelating unit, **L4** and **L5** gave complexes that are eightfold (**Re4**) and ninefold (**Re5**) less potent than the free conjugates, respectively. The only exception is the match pair **L6**/**Re6**, in which the inhibitory potency of **L6** increased moderately after metallation, following the trend previously observed for the match pairs **L1**/**Re1**, **L2**/**Re2,** and **L3**/**Re3**. The cell assays with LPS-activated macrophages corroborate the main conclusions drawn from the enzymatic assays with purified iNOS. Moreover, the inhibitory potency of **Re4** and **Re5** is comparable to that of **Re1** and **Re2**, respectively, which share the same iNOS-recognizing moieties. On the contrary, and despite having the same iNOS-recognizing moiety, complex **Re6** is 46-fold less potent than the previously described complex **Re3**. We have also performed protein–ligand dockings followed by MD simulations to establish a preliminary structure–affinity relationship. The high affinity of **L4** ($K_\mathrm{i} = 29\ \mu\mathrm{M}$) and **L5** ($K_\mathrm{i} = 6\ \mu\mathrm{M}$) for the enzyme is consistent with the higher number of stable electrostatic and H-bond interactions observed between the dap chelating unit and the protein, mainly the heme carboxylate arms. The more flexible spacer of **L5** (eihgt carbon atoms), compared to **L4** (three carbon atoms), improves these interactions. In the case of **L6** (11 carbon linker, **L6** = 759 $\mu\mathrm{M}$), the linker is too long for the accommodation of the dap chelator near the heme carboxylate arms resulting in a decrease in the binding affinity. Metallation of **L4** and **L5** led to complexes with lower affinity, which was assigned to the formation of a lower number of weaker interactions in comparison with the **L4**:iNOS and **L5**:iNOS complexes. The higher inhibitory potency found for **Re5** ($K_\mathrm{i} = 57\ \mu\mathrm{M}$), compared to **Re4** ($K_\mathrm{i} = 240\ \mu\mathrm{M}$), is likely due to the higher bulkiness of the organometallic tail of **Re5**, which provides a more extensive contact surface area than the smaller organometallic tail of **Re4**. Moreover, the absence of strong anchoring interactions in **Re4** (e.g., the $\mathrm{CO_2^-}$ group of the N^ω-$\mathrm{NO_2}$-L-Arg moiety present in **Re5**) also contributes for the fourfold lower affinity toward iNOS. In the case of **Re6,** its longer organometallic tail is not accommodated within the constrained interior of the binding pocket and is oriented toward the peripheral pocket situated at the surface of the active site. Such orientation is triggered by electrostatic repulsions observed between the $\mathrm{CO_2^-}$ group of dap-$\mathrm{Re(CO)_3}$ and the heme carboxylate group. Finally, the striking difference in inhibitory potency observed for complexes **Re6** ($K_\mathrm{i} = 258\ \mu\mathrm{M}$) and **Re3** ($K_\mathrm{i} = 6\ \mu\mathrm{M}$), which share a common NOS-recognizing unit but are stabilized by chelators of different nature (**Re6:** dap based; **Re3:** pyrazolyl-diamine based), could be rationalized by the previously described repulsions. Due to the less polar and more lipophilic character of the pyrazolyl chelator in **Re3,** the $\mathrm{Re(CO)_3}$ core is not expelled from the active pocket of iNOS by repulsion, making strong interactions with the residues Arg260 and Arg382 (34).

Following our previous work, herein we described a new family of rhenium complexes stabilized by a dap chelator coupled to the same iNOS-recognizing moiety. Changing the chelator, we expected to confer different physicochemical properties to the metal complexes which could result in improved affinities to iNOS. We observed that the non-metallated conjugates have moderate affinities for iNOS; however, the metallated compounds bind weaker to iNOS than the previously described pyrazolyl-diamine-based complexes. Using a computational approach, we have identified structural determinants that are potentially responsible for the different iNOS-recognizing abilities of the different complexes. Based on these results, it is possible to envision the design of novel '$\mathrm{MCO_3}$' complexes (M = Re/$^{99\ \mathrm{m}}$Tc) that could interact more strongly with the enzyme.

The use of metal complexes as templates for the design of metal-based probes or drug candidates is under intense research over the last years (84–86). The metal is supposed to help in the organization of the co-ordinating ligands in the three-dimensional space improving the complementarity with the targeted protein pockets (86). Herein, we have also explored this concept and demonstrated that the insertion of a metal core in an organic scaffold has significant impact in the binding affinity for an enzyme. Brought together, such knowledge provides interesting opportunities for building various structures that complement molecular diversity created by purely organic molecules (86).

Acknowledgments

This work was supported by the Fundação para a Ciência e Tecnologia (FCT), Portugal, through projects

PTDC/QUI-QUI/121752/2010 and EXCL/QEQ-MED/0233/2012. C^{2}TN/IST authors gratefully acknowledge the FCT support through the UID/Multi/04349/2013 project. M. Morais and B. L. Oliveira thank FCT for Ph.D. fellowships (SFRH/BD/48066/2008 and SFRH/BD/38753/2007, respectively). I. S. Moreira is supported by FCT Ciência 2008 (Hiring of PhDs for the SCTN - financed by POPH - QREN - Typology 4.2 - Promoting Scientific Employment, co-financed by MES National Funding and The European Social Fund). Covidien-Mallinckrodt is acknowledged for the IsoLink kits and Dr. J. Marçalo for performing the ESI-MS analyses. The ESI/QITMS was acquired with the support of the Programa Nacional de Reequipamento Científico of FCT and is part of RNEM-Rede Nacional de Espectrometria de Massa also supported by FCT.

References

1. Moncada S., Palmer R.M.J., Higgs E.A. (1991) Nitric-Oxide – physiology, pathophysiology, and pharmacology. Pharmacol Rev;43:109–142.
2. Kerwin J.F., Lancaster J.R., Feldman P.L. (1995) Nitric-Oxide – a new paradigm for 2nd-messengers. J Med Chem;38:4343–4362.
3. Wink D.A., Mitchell J.B. (2003) Nitric oxide and cancer: an introduction. Free Radical Biol Med;34:951–954.
4. Duncan A.J., Heales S.J.R. (2005) Nitric oxide and neurological disorders. Mol Aspects Med;26:67–96.
5. Lechner M., Lirk P., Rieder J. (2005) Inducible nitric oxide synthase (iNOS) in tumor biology: the two sides of the same coin. Semin Cancer Biol;15:277–289.
6. Fukumura D., Kashiwagi S., Jain R.K. (2006) The role of nitric oxide in tumour progression. Nat Rev Cancer;6:521–534.
7. Hong H., Sun J.T., Cai W.B. (2009) Multimodality imaging of nitric oxide and nitric oxide synthases. Free Radical Biol Med;47:684–698.
8. Salerno L., Sorrenti V., Di Giacomo C., Romeo G., Siracusa M.A. (2002) Progress in the development of selective nitric oxide synthase (NOS) inhibitors. Curr Pharm Des;8:177–200.
9. Zhang J., McCarthy T.J., Moore W.M., Currie M.G., Welch M.J. (1996) Synthesis and evaluation of two positron-labeled nitric oxide synthase inhibitors, S- C-11 methylisothiourea and S-(2- F-18 fluoroethyl)isothiourea, as potential positron emission tomography tracers. J Med Chem;39:5110–5118.
10. Nagano T., Yoshimura T. (2002) Bioimaging of nitric oxide. Chem Rev;102:1235–1269.
11. Panda K., Chawla-Sarkar M., Santos C., Koeck T., Erzurum S.C., Parkinson J.F., Stuehr D.J. (2005) Visualizing inducible nitric-oxide synthase in living cells with a heme-binding fluorescent inhibitor. Proc Natl Acad Sci USA;102:10117–10122.
12. Dunn A.R., Belliston-Bittner W., Winkler J.R., Getzoff E.D., Stuehr D.J., Gray H.B. (2005) Luminescent ruthenium(II)- and rhenium(I)-diimine wires bind nitric oxide synthase. J Am Chem Soc;127:5169–5173.
13. Zhou D., Lee H., Rothfuss J.M., Chen D.L., Ponde D.E., Welch M.J., Mach R.H. (2009) Design and synthesis of 2-amino-4-methylpyridine analogues as inhibitors for inducible nitric oxide synthase and *in vivo* evaluation of (18)F 6-(2-fluoropropyl)-4-methyl-pyridin-2-amine as a potential PET tracer for inducible nitric oxide synthase. J Med Chem;52:2443–2453.
14. Oliveira B.L., Raposinho P.D., Mendes F., Santos I.C., Santos I., Ferreira A., Cordeiro C., Freire A.P, Correia J.D.G. (2011) Targeting nitric oxide synthase with Tc-99 m/Re-tricarbonyl complexes containing pendant guanidino or isothiourea moieties. J Organomet Chem;696:1057–1065.
15. Oliveira B.L., Raposinho P.D., Mendes F., Figueira F., Santos I., Ferreira A., Cordeiro C., Freire A.P, Correia J.D.G. (2010) Re and Tc tricarbonyl complexes: from the suppression of NO biosynthesis in macrophages to *in vivo* targeting of inducible nitric oxide synthase. Bioconjug Chem;21:2168–2172.
16. Oliveira B.L., Correia J.D.G., Raposinho P.D., Santos I., Ferreira A., Cordeiro C., Freire A.P. (2009) Re and 99 mTc organometallic complexes containing pendant l-arginine derivatives as potential probes of inducible nitric oxide synthase. Dalton Trans;152–162.
17. Liu Y., Oliveira B.L., Correia J.D.G., Santos I.C., Santos I., Spingler B., Alberto R. (2010) Syntheses of bifunctional 2,3-diamino propionic acid-based chelators as small and strong tripod ligands for the labelling of biomolecules with 99 mTc. Org Biomol Chem;8:2829–2839.
18. Oliveira B.L., Liu Y., Correia JoDG, Santos I., Gano L., Spingler B., Alberto R. (2010) 2,3-Diamino propionic acid based chelators for labeling biomolecules with 99 mTc(I). Nucl Med Biol;37:704.
19. Shen Y.J., Schottelius M., Zelenka K., De Simone M., Pohle K., Kessler H., Wester H.J., Schmutz P., Alberto R. (2013) Orthogonally protected artificial amino acid as tripod ligand for automated peptide synthesis and labeling with Tc-99m(OH2)(3)(CO)(3) (+). Bioconjug Chem;24:26–35.
20. Liu Y., Pak J.K., Schmutz P., Bauwens M., Mertens J., Knight H., Alberto R. (2006) Amino acids labeled with Tc-99m(CO)(3) (+) and recognized by the L-type amino acid transporter LAT1. J Am Chem Soc;128:15996–15997.
21. Correia J.D.G., Paulo A., Raposinho P.D., Santos I. (2011) Radiometallated peptides for molecular imaging and targeted therapy. Dalton Trans;40:6144–6167.
22. Morais M., Paulo A., Gano L., Santos I., Correia J.D.G. (2013) Target-specific Tc(CO)(3)-complexes for *in vivo* imaging. J Organomet Chem;744:125–139.
23. Yu G., Wang S.Z., Wang K., Hu Y.F., Hu H.W. (2004) A novel approach to 1,2-dihydro-2-oxo-3-pyridinecarboxylic ester via aromatization induced by deamidation. Synthesis (Stuttg);7:1021–1028.

24. Alberto R., Egli A., Abram U., Hegetschweiler K., Gramlich V., Schubiger P.A. (1994) Synthesis and reactivity of [NEt4]2[ReBr3(CO)3]. Formation and structural characterization of the clusters [NEt4][Re3 (m3-OH)(m-OH)3(CO)9] and [NEt4][Re2(m-OH)3(CO)6] by alkaline treatment. J Chem Soc, Dalton Trans; 281:5–20.
25. Lazarova N., James S., Babich J., Zubieta J. (2004) A convenient synthesis, chemical characterization and reactivity of [Re(CO)(3)(H2O)(3)]Br: the crystal and molecular structure of [Re(CO)(3)(CH3CN)(2)Br]. Inorg Chem Commun;7:1023–1026.
26. Hevel J.M.M.M. (1994) Nitric-oxide synthase assays. Methods Enzymol;233:250–258.
27. Archer S. (1993) Measurement of nitric oxide in biological models. FASEB J;7:349–360.
28. Wolff D.J., Gauld D.S., Neulander M.J., Southan G. (1997) Inactivation of nitric oxide synthase by substituted aminoguanidines and aminoisothioureas. J Pharmacol Exp Ther;283:265–273.
29. Eisenthal R., Cornish-Bowden A. (1974) The direct linear plot. A new graphical procedure for estimating enzyme kinetic parameters. Biochem J;139:715–720.
30. Green L.C., Wagner D.A., Glogowski J., Skipper P.L., Wishnok J.S., Tannenbaum S.R. (1982) Analysis of nitrate, nitrite, and [15N]nitrate in biological fluids. Anal Biochem;126:131–138.
31. Tim M. (1983) Rapid colorimetric assay for cellular growth and survival: application to proliferation and cytotoxicity assays. J Immunol Methods;65:55–63.
32. Fedorov R., Hartmann E., Ghosh D.K., Schlichting I. (2003) Structural basis for the specificity of the nitric-oxide synthase inhibitors W1400 and Nω-Propyl-l-Arg for the inducible and neuronal isoforms. J Biol Chem;278:45818–45825.
33. Oliveira B.L., Moreira I.S., Fernandes P.A., Ramos M.J., Santos I., Correia J.D.G. (2013) Insights into the structural determinants for selective inhibition of nitric oxide synthase isoforms. J Mol Model;19:1537–1551.
34. Oliveira B.L., Moreira I.S., Fernandes P.A., Ramos M.J., Santos I., JoDG Correia (2013) Theoretical studies on the binding of rhenium(I) complexes to inducible nitric oxide synthase. J Mol Graph Model;45:13–25.
35. Morris G.M., Goodsell D.S., Halliday R.S., Huey R., Hart W.E., Belew R.K., Olson A.J. (1998) Automated docking using a Lamarckian genetic algorithm and an empirical binding free energy function. J Comput Chem;19:1639–1662.
36. Morris G.M., Huey R., Lindstrom W., Sanner M.F., Belew R.K., Goodsell D.S., Olson A.J. (2009) AutoDock4 and AutoDockTools4: automated docking with selective receptor flexibility. J Comput Aided Mol Des;21:681–691.
37. Shelley J., Cholleti A., Frye L., Greenwood J., Timlin M., Uchimaya M. (2007) EPIK: a software program for prediction and protonation state generation for drug-like molecules. J Comput Aided Mol Des;21:681–691.
38. Raman C.S., Li H., Martasek P., Southan G., Masters B.S.S., Poulos T.L. (2001) Crystal structure of nitric oxide synthase bound to nitro indazole reveals a novel inactivation mechanism. Biochemistry;40:13448–13455.
39. Ziegler T. (1991) Approximate density functional theory as a practical tool in molecular energetics and dynamics. Chem Rev;91:651–667.
40. Becke A.D. (1993) Density-functional thermochemistry. III. The role of exact exchange. J Chem Phys;98:5648–5652.
41. Sousa S.F., Fernandes P.A., Ramos M.J. (2007) General performance of density functionals. J Phys Chem A;111:10439–10452.
42. Lee C., Yang W., Parr R.G. (1988) Development of the Colle-Salvetti correlation-energy formula into a functional of the electron density. Phys Rev B Condens Matter;37:785.
43. Vanommeslaeghe K., Hatcher E., Acharya C., Kundu S., Zhong S., Shim J., Darian E., Guvench O., Lopes P., Vorobyov I., Mackerell A.D. Jr. (2010) CHARMM general force field: a force field for drug-like molecules compatible with the CHARMM all-atom additive biological force fields. J Comput Chem;31:671–690.
44. Li X., Liu X., Wu Z., Zhang H. (2008) DFT/TDDFT studies on the electronic structures and spectral properties of Rhenium(I) pyridinybenzoimidazole complexes. J Phys Chem A;112:11190–11197.
45. Bayly C.I., Cieplak P., Cornell W., Kollman P.A. (1993) A well-behaved electrostatic potential based method using charge restraints for deriving atomic charges: the RESP model. J Phys Chem;97:10269–10280.
46. Cornell W.D., Cieplak P., Bayly C.I., Kollmann P.A. (1993) Application of RESP charges to calculate conformational energies, hydrogen bond energies, and free energies of solvation. J Am Chem Soc;115:9620–9631.
47. Connolly M. (1983) Analytical molecular surface calculation. J Appl Crystallogr;16:548–558.
48. Andrae D., Häußermann U., Dolg M., Stoll H., Preuß H. (1990) Energy-adjustedab initio pseudopotentials for the second and third row transition elements. Theor Chim Acta;77:123–141.
49. Dunning T.H. Jr, Hay P.J., editors (1976) Modern Theoretical Chemistry. H. F. Schaefer III edn. New York: Plenum.
50. Dolg M., Wedig U., Stoll H., Preuss H. (1987) Energy-adjusted abinitio pseudopotentials for the first row transition elements *J*. Chem Phys;86:866–873.
51. Dupradeau F.-Y., Pigache A., Zaffran T., Savineau C., Lelong R., Grivel N., Lelong D., Rosanski W., Cieplak P. (2010) The R.E.D. tools: advances in RESP and ESP charge derivation and force field library building. Phys Chem Chem Phys;12:7821–7839.
52. Dupradeau F.-Y., Cézard C., Lelong R., Stanislawiak É., Pêcher J., Delepine J.C., Cieplak P. (2008) R.E.DD.B.: a database for RESP and ESP atomic

charges, and force field libraries. Nucleic Acids Res;36:D360–D367.
53. Vanquelef E., Simon S., Marquant G., Garcia E., Klimerak G., Delepine J.C., Cieplak P., Dupradeau F.Y. (2011) R.E.D. server: a web service for deriving RESP and ESP charges and building force field libraries for new molecules and molecular fragments. Nucleic Acids Res;39:W511–W517.
54. Mayo S.L., Olafson B.D., Goddard W.A. (1990) DREIDING: a generic force field for molecular simulations. J Phys Chem;94:8897–8909.
55. Hansen L., Cini R., Taylor A., Marzilli L.G. (1992) Rhenium(V) oxo complexes relevant to technetium renal imaging agents derived from mercaptoacetylglycylglycylaminobenzoic acid isomers. Structural and molecular mechanics studies. Inorg Chem;31:2801–2808.
56. Marzilli L.G., Banaszczyk M.G., Hansen L., Kuklenyik Z., Cini R., Taylor A. Jr (1994) Linking deprotonation and denticity of chelate ligands. Rhenium(V) oxo analogs of technetium-99m radiopharmaceuticals containing N2S2 chelate ligands. Inorg Chem;33: 4850–4860.
57. Hancock R.D., Reichert D.E., Welch M.J. (1996) Molecular mechanics force field for modeling technetium(V) complexes. Inorg Chem;35:2165–2166.
58. Cundari T.R., Fu W. (2000) Genetic algorithm optimization of a molecular mechanics force field for technetium. Inorg Chim Acta;300–302:113–124.
59. Reichert D.E., Welch M.J. (2001) Applications of molecular mechanics to metal-based imaging agents. Coord Chem Rev;212:111–131.
60. Wolohan P., Reichert D.E. (2007) CoMSIA and docking study of rhenium based estrogen receptor ligand analogs. Steroids;72:247–260.
61. Comba P., Daubinet A., Martin B., Pietzsch H.-J., Stephan H. (2006) A new molecular mechanics force field for the design of oxotechnetium(V) and oxorhenium(V) radiopharmaceuticals. J Organomet Chem;691:2495–2502.
62. Desbouis D., Struthers H., Spiwok V., Küster T., Schibli R. (2008) Synthesis, *in vitro*, and *in silico* evaluation of organometallic technetium and rhenium thymidine complexes with retained substrate activity toward human thymidine kinase type 1. J Med Chem;51:6689–6698.
63. James S., Maresca K.P., Allis D.G., Valliant J.F., Eckelman W., Babich J.W., Zubieta J. (2006) Extension of the single amino acid chelate concept (SAAC) to bifunctional biotin analogues for complexation of the M (CO)3 + 1 Core (M = Tc and Re): syntheses, characterization, biotinidase stability, and avidin binding. Bioconjug Chem;17:579–589.
64. Hoops S.C., Anderson K.W., Merz K.M. (1991) Force field design for metalloproteins. J Am Chem Soc;113:8262–8270.
65. Peters M.B., Yang Y., Wang B., Füsti-Molnár L.S., Weaver M.N., Merz K.M. (2010) Structural survey of zinc-containing proteins and development of the zinc AMBER force field (ZAFF). J Chem Theory Comput;6:2935–2947.
66. Sousa S., Fernandes P., Ramos M. (2007) Effective tailor-made force field parameterization of the several Zn coordination environments in the puzzling FTase enzyme: opening the door to the full understanding of its elusive catalytic mechanism. Theor Chem Acc;117:171–181.
67. Norrby P.-O., Brandt P. (2001) Deriving force field parameters for coordination complexes. Coord Chem Rev;212:79–109.
68. Phillips J.C., Braun R., Wang W., Gumbart J., Tajkhorshid E., Villa E., Chipot C., Skeel R.D., Kalé L., Schulten K. (2005) Scalable molecular dynamics with NAMD. J Comput Chem;26:1781–1802.
69. MacKerell A.D., Bashford D., Bellott Dunbrack R.L., Evanseck J.D., Field M.J., Fischer S. *et al.* (1998) All-atom empirical potential for molecular modeling and dynamics studies of proteins. J Phys Chem B;102:3586–3616.
70. Cho K.-B., Derat E., Shaik S. (2007) Compound I of nitric oxide synthase: the active site protonation state. J Am Chem Soc;129:3182–3188.
71. Dolinsky T.J., Nielsen J.E., McCammon J.A., Baker N.A. (2004) PDB2PQR: an automated pipeline for the setup of Poisson-Boltzmann electrostatics calculations. Nucleic Acids Res;32:W665–W667.
72. Li H., Robertson A.D., Jensen J.H. (2005) Very fast empirical prediction and rationalization of protein pKa values. Proteins: Struct, Funct, Bioinf;61:704–721.
73. Dolinsky T.J., Czodrowski P., Li H., Nielsen J.E., Jensen J.H., Klebe G., Baker N.A. (2007) PDB2PQR: expanding and upgrading automated preparation of biomolecular structures for molecular simulations. Nucleic Acids Res;35:W522–W525.
74. Humphrey W., Dalke A., Schulten K. (1996) VMD: visual molecular dynamics. J Mol Graph;14:33–38.
75. Essmann U., Perera L., Berkowitz M.L., Darden T., Lee H., Pedersen L.G. (1995) A smooth particle mesh Ewald method. J Chem Phys;103:8577–8593.
76. Grest G.S., Kremer K. (1986) Molecular dynamics simulation for polymers in the presence of a heat bath. Phys Rev A;33:3628.
77. Hoover W.G. (1985) Canonical dynamics: equilibrium phase-space distributions. Phys Rev A;31:1695.
78. Feller S.E., Zhang Y., Pastor R.W., Brooks B.R. (1995) Constant pressure molecular dynamics simulation: the Langevin piston method. J Chem Phys;103:4613–4621.
79. Nosé S. (2002) A molecular dynamics method for simulations in the canonical ensemble. Mol Phys;100:191–198.
80. DeLano W.L., editor (2002) The PyMOL Molecular Graphics System. San Carlos, CA, USA: DeLano Scientific.
81. Alberto R., Ortner K., Wheatley N., Schibli R., Schubiger A.P. (2001) Synthesis and properties of boranocarbonate: a convenient *in situ* CO source for the

aqueous preparation of (TC)-T-99m(OH2)(3)(CO)(3) (+). J Am Chem Soc;123:3135–3136.
82. Alberto R. (2010) Organometallic Radiopharmaceuticals. In: Jaouen G., MetzlerNolte N., editors. Organometallic Radiopharmaceuticals. Berlin: Springer-Verlag Berlin; p. 219–246.
83. Cornish-Bowden A. (1975) The use of the direct linear plot for determining initial velocities. Biochem J;149:305–312.
84. Almeida A., Oliveira B., Correia J.D.G., Soveral G., Casini A. (2013) Emerging protein targets for metal-based pharmaceutical agents: an update. Coord Chem Rev;257:2689–2704.
85. Mjos K.D., Orvig C. (2014) Metallodrugs in medicinal inorganic chemistry. Chem Rev;118:4540–4563.
86. Dörr M., Meggers E. (2014) Metal complexes as structural templates for targeting proteins. Curr Opin Chem Biol;19:76–81.
87. Seo J., Igarashi J., Li H.Y., Martasek P., Roman L.J., Poulos T.L., Silverman R.B. (2007) Structure-based design and synthesis of N-omega-nitro-L-arginine-containing peptidomimetics as selective inhibitors of neuronal nitric oxide synthase. Displacement of the heme structural water. J Med Chem;50:2089–2099.

Supporting Information

Additional Supporting Information may be found in the online version of this article:

Scheme S1: Synthesis of precursor 4.

Figure S1. Binding site residues of iNOS considered flexible during the docking process.

Figure S2. Lowest-energy conformations of the docked compounds L4–L6 and Re4–Re6.

Figure S3–S8: Top 10 (or 12) lowest-energy (kcal/mol) conformations obtained from the docking of the inhibitors L4–L6 and Re4–Re6 in the active pocket of iNOS.

Figure S9. Overall Root-Mean-Square Deviation (RMSD) of the protein backbone over 8 ns simulation for the systems Re4:iNOS, Re5:iNOS and Re6:iNOS.

Figure S10. RMSD of L4, L5 and L6 for each simulation.

Figure S11. RMSD of the free complexes Re4–Re6 during 8 ns simulation.

Figure S12: Temporal evolution of the RMSD of Re6 from the initial structure during the 15 ns of simulation.

Figure S13. Plots of the number of H-bonds between iNOS and L5 or L6 during the last 3 ns of simulation.

Figure S14. Putative hydrogen bonding networks at the active site of L5:iNOS and L6:iNOS.

Figure S15. Superimposition of snapshots at 0 ns and 8 ns of simulation of the complexes Re4:iNOS, Re5:iNOS, and Re6:iNOS.

Figure S16. Proposed structure of Re3 in complex with iNOS obtained by MD simulation.

Figure S17. Scheme of ligands L4–L6 and rhenium complexes Re4–Re6 and correspondent torsions free to rotate during the docking process.

Figure S18. Building blocks involved in charge derivation of L5, L6, Re5 and Re6.

Table S1. Distances observed between the O atoms of Glu371 and the nitrogen atoms Nε and Nη1 of the NO_2-guanidine moiety.

Table S2. Occupancy (in %) of intermolecular hydrogen bonds for L5 and L6 for the last 3 ns of simulation.